CrystEngComm

PAPER

Investigating the Crystal Engineering of the Pillared Paddlewheel Metal-Organic Framework $Zn_2(NH_2BDC)_2DABCO$

Received 00th January 20xx,
Accepted 00th January 20xx

DOI: 10.1039/x0xx00000x

www.rsc.org/

D. T. McGrath,[a] V. A. Downing [a] and M. J. Katz [a,*]

The synthesis of $Zn_2(NH_2BDC)_2DABCO$ was investigated with the hopes of producing a material with a high surface area. Despite considerable efforts to get reproducible results, replacing BDC with NH_2BDC was not trivial; the gas adsorption isotherms were inconsistent, resulting in different gas uptakes and large variation in hysteresis loops. Given this, we examined the gas adsorption isotherms (BET surface area and pore size distributions), the solution-phase NMR, and the powder X-ray diffractograms of our materials in order to puzzle out the underlying chemistry. From this data, we illustrate how 1D chains of $Zn(H_2O)_2(NH_2BDC)$ are converted to partially pillared $Zn_2(NH_2BDC)_2DABCO$ which is either amorphous or crystalline based on the NH_2BDC:DABCO ratio.

1 Introduction

Metal-organic frameworks (MOFs) are a class of porous materials made up of a combination of inorganic metal nodes and organic linkers.[1-4] Once assembled, one of the unifying features of MOFs is that a considerable amount of unused space – space that is not occupied by the node and linker – remains behind. This porous nature and the concomitant high surface area associated with MOFs allow for utilization in a wide variety of applications such as gas storage and separation,[5-8] chemical sensing,[9-12] and catalysis.[13-17]

The other attractive feature of MOF research is that the porous space can be tailored towards applications with judicious choice of both node and linker.[18,19] For this reason, the utilization of functionalized linkers has become prevalent in MOF chemistry. For example, when the 2-aminoterephthalic acid linker (NH_2BDC) was used in place of the amine-free terephthalic acid linker (BDC) in the MOF UiO-66, then improved capturing of carbon dioxide,[20] selective removal of toxic chemicals,[21] and applications in fluorescence imaging in cancer therapy were observed.[22]

While the properties associated with these changes are often of interest, the determination of the synthetic pathways necessary to form these materials is often of great frustration. The juxtaposition of the need for new materials coupled to the challenges associated with synthesis of new materials is the cornerstone of crystal engineering. To that end, researchers have spent considerable effort to investigate synthetic strategies to target the de novo synthesis of MOFs.[23-26] Congruently, post-synthesis methods have also been widely investigated.[27-31] In these methods, the existing MOF undergoes a node/linker substitution, or a chemical reaction, to introduce the desired functionalities into the porous structure.[31-37]

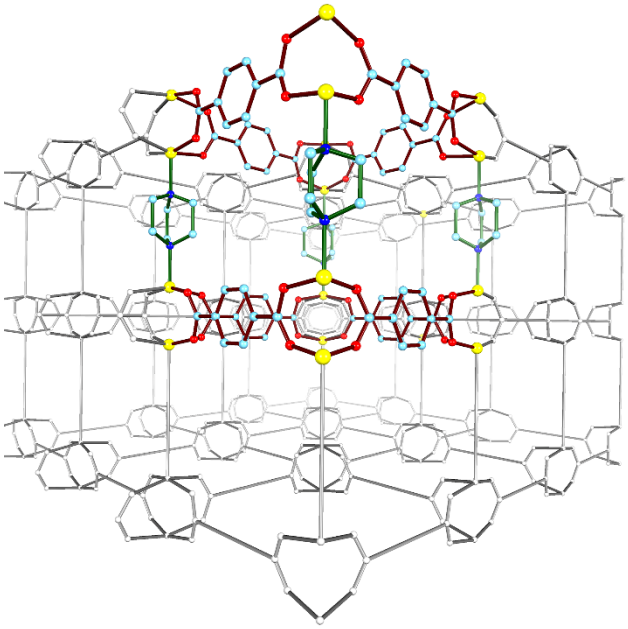

Fig. 1 Crystal structure of $Zn_2(NH_2BDC)_2DABCO$ illustrating how pairs of zinc cations connect to one another via BDC units (dark red bonds) to form a paddlewheel $(Zn_2COOR)_4$ sheet. These sheets connect to one another via a DABCO pillar (dark green bonds) to form the overall pillared paddlewheel MOF. Zinc (yellow), oxygen (red), carbon (light blue), nitrogen (dark blue). Amino groups have been omitted for clarity.

With this in mind, we have been investigating the synthesis, properties, and applications of MOFs.[38-41] Recently, we have turned our attention to amine-functionalized MOFs due to the observation that amine-containing MOFs seem to outperform their parent complex in catalysis and gas adsorption properties.[42,43] Furthermore, amine-functionalized MOFs offer an easy method for post-synthesis processes.[44-46] To our surprise, the

[a] Department of Chemistry, Memorial University of Newfoundland, 230 Elizabeth Avenue, St. John's, Newfoundland and Labrador, Canada

Electronic Supplementary Information (ESI) available: [details of any supplementary information available should be included here]. See DOI: 10.1039/x0xx00000x

amine-functionalized $Zn_2(NH_2BDC)_2DABCO$ (DABCO = 1,4-diazabicyclo[2.2.2]octane) has not been extensively investigated for these properties (Fig. 1).[47]

Interestingly, the Brunauer–Emmett–Teller (BET) surface area of $Zn_2(NH_2BDC)_2DABCO$ is considerably lower than that of the parent MOF, 1320 – 1510 m^2/g vs. 1700 – 1950 m^2/g respectively.[37,40,47-49] Given this, we initially set out to understand the synthetic factors that affect the crystal engineering of $Zn_2(NH_2BDC)_2DABCO$. Although, ultimately, we were not able to determine how to optimize the synthesis of $Zn_2(NH_2BDC)_2DABCO$ to achieve a high and reproducible surface area, the challenges faced yielded a unique opportunity to gain insights into the formation process of pillared paddlewheel MOFs.

2 Experimental method

2.1 Reagents

All the chemicals used were reagent grade and used as-received. Reagents used were zinc nitrate hexahydrate ($Zn(NO_3)_2•6H_2O$), 2-aminoterephthalic acid, 1,4-diazabicyclo[2.2.2]octane, *N,N*-dimethylformamide (DMF), ethanol, *N,N*-diethylformamide (DEF), and nitric acid (HNO_3).

2.2 Instrumentation

For gas adsorption analysis, samples were placed in sample holders using a filler rod to reduce the unoccupied volume, and a seal frit to prevent unwanted guest molecules from interacting with the samples prior to analysis. Before any measurements, samples were thermally degassed (activated) on a Micromeretics Smart VacPrep gas adsorption sample preparation instrument. Samples were initially heated at 90°C while a vacuum level below 1.00 mmHg was reached at 5.00 mmHg/s. Subsequently, the samples were heated to 150°C for 500 min under unrestricted vacuum. The samples were cooled to room temperature and the sample holder was backfilled with $N_{2(g)}$. Gas adsorption isotherm data was collected at 77 K on a Micromeritics 3Flex Surface Characterization instrument using $N_{2(g)}$ as the probe molecule. Using the MicroActive software suite, the data obtained was used to determine the BET surface area[50] and pore size distributions (PSD).

For ^1H NMR data, MOF samples were dissolved by first adding 3 drops of D_2SO_4 to approximately 5 mg of sample. Once dissolved, 1 mL of DMSO-d_6 was added and used as the lock solvent. ^1H NMR data was collected on a 500 MHz Bruker Avance III instrument using an inverse probe.

Powder X-ray diffraction (PXRD) patterns were acquired using a Rigaku Ultima IV X-ray diffractometer equipped with a copper X-ray source operating at 40 kV x 44 mA (1.76 kW) and a scintillation counter detector. A continuous scan mode between $2\theta = 5° – 30°$ with a sampling width of 0.020° and a scan rate of 1.000°/min was utilized.

Scanning Electron Microscope (SEM) images were collected on a JEOL JSM 7100 F SEM using a thermally-assisted Schottky-type Field Emission gun as the electron source. All samples were carbon coated prior to analysis.

2.3 Synthesis of $Zn_2(NH_2BDC)_2DABCO$

Samples were synthesized based on a similar prep by Dybtsev et al. for $Zn_2(BDC)_2DABCO$.[51] 0.0947 g (0.844 mmoles) of DABCO was dissolved in 7 mL of DMF in a 30 mL DURAN bottle and sonicated to dissolution (approximately 30-45 s). To this, 0.5010 g (1.684 mmoles) of $Zn(NO_3)_2•6H_2O$ was added along with an additional 7 mL of DMF. The samples were subsequently sonicated to dissolution (approximately 30-45 s). Finally, 0.2765 g (1.526 mmoles) of NH_2BDC was added along with an additional 7 mL aliquot of DMF. The samples were sonicated until dissolution (approximately 30-45 s) and placed in an oven set at 120°C for 48 h. Modifications made to this synthetic procedure in an attempt to optimize the surface area included changes in mole ratio, heating conditions, and solvent choice (refer to Table S1 in the Electronic Supplementary Information (ESI)).

After 48 h, the samples were removed from the oven and cooled for approximately 5 min at room temperature. Crystals were broken loose from the DURAN bottle with a flat-tipped spatula, ensuring crystals from the solvent ring were not incorporated into the bulk sample, as they are likely unrepresentative of the target product. The loose crystalline material was transferred to a 50 mL centrifuge tube and centrifuged for 5 min at 5000 rpm. After centrifugation, the mother liquor was decanted and the solid crystalline samples were washed with three separate 10 mL aliquots of fresh DMF, followed by three 10 mL aliquots of methanol; the samples were centrifuged for 5 min at 5000 rpm between washes. Subsequently, samples were dried for 45 min in a vacuum oven at 80°C to remove surface-bound solvent.

3 Results

3.1 Synthesis

The initial investigation into discovering and optimizing a facile de novo synthesis for $Zn_2(NH_2BDC)_2DABCO$ originated from previous knowledge regarding the usefulness of amine-functionalized MOFs (e.g. UiO-66-NH_2 and NH_2-MIL-101(Al)).[43,52] Initially, without experimental modification, a BET surface area of 950 m^2/g was obtained; this is considerably lower than the 1320 m^2/g observed by Dybtsev et al.[37]

With this in mind, several attempts were made to modify the synthetic procedure in order to improve the porosity. Our various attempts can be found in Table S1 in the ESI. Unfortunately, there was no observable trend between the various factors. Even worse, seemingly identical procedures gave non-reproducible results. For instance, in one batch of samples where the role of the NH_2BDC was being investigated, an increase in the NH_2BDC mole ratio up to 30% resulted in a BET surface area increase from 950 m^2/g to 1400 m^2/g (Table S1 in the ESI). Although this data seemed promising, frustratingly, any attempt to reproduce the data resulted in BET surface areas ranging from 500 – 1000 m^2/g.

3.2 Gas adsorption isotherms

Fig. 2 illustrates some of the variability in gas adsorption that we observed during the synthesis of $Zn_2(NH_2BDC)_2DABCO$.

There are two main features of these isotherms. Firstly, the gas uptake of all these materials varies considerably. Secondly, nearly all the samples show some degree of hysteresis. This indicates the presence of a mesoporous material; $Zn_2(NH_2BDC)_2DABCO$ is not expected to contain mesopores. However, the magnitude of the hysteresis, as well as the shape of the hysteresis, varied considerably. This suggests that the mesoporous material is not due to a highly ordered system.

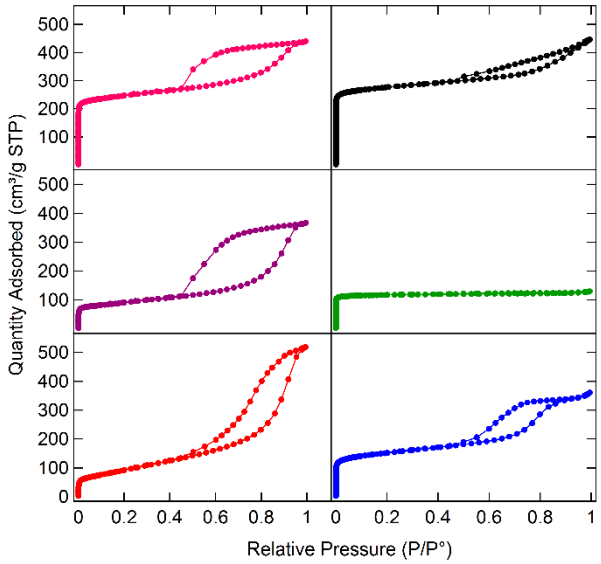

Fig. 2 Selected N_2 gas adsorption isotherms of various samples of $Zn_2(NH_2BDC)_2DABCO$ synthesized in this work. The various gas adsorption isotherms illustrate the range of gas uptake and hysteresis that was observed.

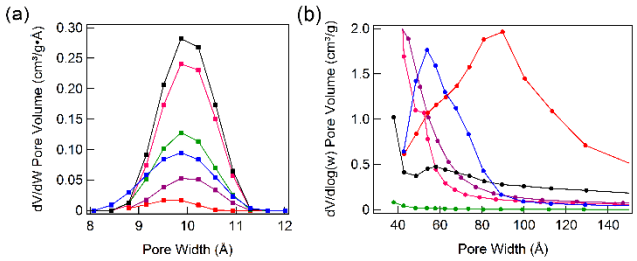

Fig. 3 (a) DFT-PSD of the isotherms in Fig. 2 of $Zn_2(NH_2BDC)_2DABCO$. The similar pore size is consistent with the presence of $Zn_2(NH_2BDC)_2DABCO$. (b) BJH-PSD of the desorption branch of the isotherms in Fig 2. The different hysteresis loops are associated with different sized mesopores. The BJH-PSD for the adsorption branch can be seen in Fig. S1 of the ESI.

To better understand these samples, the PSD of the samples in Fig. 2 were analyzed (Fig. 3). For the micropores (Fig. 3a), density functional theory (DFT) was utilized. For all the samples, a 10 Å PSD was obtained. The value of the PSD is consistent with what would be expected for the pore size for $Zn_2(NH_2BDC)_2DABCO$, which is expected to be similar to that of the parent, $Zn_2(BDC)_2DABCO$ (9.6 Å).[53] Thus, despite the wide distribution of gas uptake and BET surface areas, the gas adsorption isotherms are consistent with the presence of $Zn_2(NH_2BDC)_2DABCO$.

For the mesopores responsible for the hysteresis, the Barrett-Joyner-Halenda (BJH) method was utilized to determine the PSD. As shown in Fig. 3b, comparing the PSD of the desorption branches demonstrates that the pore sizes are not uniformly distributed, as observed in the micropore region.

Based on the gas adsorption isotherms, it can be concluded that $Zn_2(NH_2BDC)_2DABCO$ is present and either contains a mesoporous impurity or somehow contains defects that produce mesopores.

3.3 NMR and PXRD analysis of a representative sample set

Given the challenges faced with the synthesis of $Zn_2(NH_2BDC)_2DABCO$, we turned our attention to the composition of our products. To that end, as illustrated in Fig. 4, we selected five representative samples which spanned from low surface area (260 m^2/g) to high surface area (1400 m^2/g). Table 1 illustrates the synthetic pathway used to achieve the observed BET surface area and the NMR results of the dissolved material. The Scanning Electron Microscope (SEM) images of these samples can be observed in Fig. S4. Highly insulating chunks, and rectangular prisms, consistent with the morphology of $Zn_2(NH_2BDC)_2DABCO$, are present. As the surface area increases, there is a concomitant increase in rectangular prisms and a decrease in the insulating chunks.

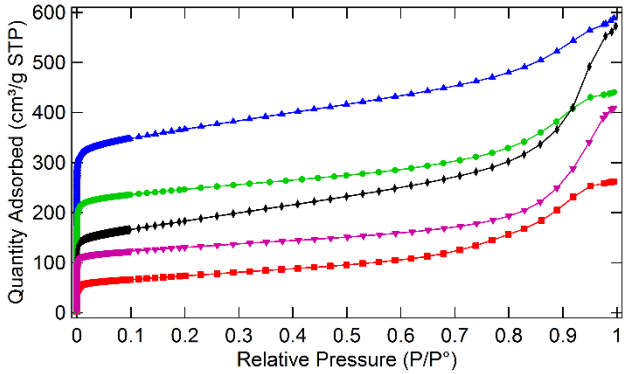

Fig. 4 N_2 gas adsorption isotherms measured at 77 K for **P1** (red squares), **P2** (purple upside-down triangles), **P3** (black diamonds), **P4** (green circles), and **P5** (blue triangles). Fig. S2 of the ESI illustrates the hysteresis observed for isotherms **P1** – **P5**.

Table 1 Comparison of BET surface areas and NMR proton ratios for five preps for $Zn_2(NH_2BDC)_2DABCO$.

	Modification[a]	BET Surface Area (m^2/g)	NMR Proton Ratio (NH_2BDC:DABCO)[b,c]
P1	+5% $Zn(NO_3)_2•6H_2O$	260	6:6.00
P2	+10% $Zn(NO_3)_2•6H_2O$	500	6:4.68
P3	+10% NH_2BDC	655	6:4.57
P4	Unmodified prep	950	6:6.60
P5	+30% NH_2BDC	1400	6:7.35

[a] Given the reproducibility challenges, this column is present to illustrate which samples were used and is not reflective of the reproducibility.

[b] The integration of NH_2BDC was set to 6, therefore an ideal ratio for $Zn_2(NH_2BDC)_2DABCO$ would be 6:12.

[c] Relaxation rates were measured to ensure accurate integrations.

3.3.1 NMR analysis

NMR analysis was carried out on all samples (see Table S1 in the ESI). Given the formula of $Zn_2(NH_2BDC)_2DABCO$, a ratio of 6:12

(NH_2BDC:DABCO), neglecting the -NH_2 and -COOH protons, is expected. To our surprise, **P1** – **P5** had an integration that was considerably lower than ideal (Table 1, and Fig. S3 in the ESI). Even **P5**, which exhibited the highest BET surface area of any sample synthesized, had a ratio of only 6:7.35. In looking at the values in Table 1 and Table S1, there is no clear relationship between BET surface area and linker ratios.

The NMR data suggests two possible extremes which may be responsible for the less than ideal linker ratios. Firstly, there may be too little DABCO in the material. It is well established that pillared paddlewheel MOFs form via the initial formation of 2D sheets followed by pillaring of sheets to form $Zn_2(NH_2BDC)_2DABCO$.[33,51] Incomplete pillaring may lead to mesoporous regions in the MOF. Furthermore, the decrease in DABCO linkers may reduce the available surface area (i.e. a decrease in DABCO units for N_2 to interact with) or simply may not produce sufficient pillars to separate the 2D sheets in regions of the crystal structure.

To the other extreme, there may be too much NH_2BDC. This would suggest that there are impurities of another material which contains NH_2BDC, but not DABCO. The impurities may be a MOF (e.g. MOF-5-NH_2) or a coordination polymer containing Zn and NH_2BDC.[54,55] MOF-5-NH_2 seems unlikely as it is porous (2040 m^2/g) and thus would produce a more porous material; therefore it is more likely that a non-porous coordination polymer is present.[56]

Ultimately, in the absence of structural insights, both extremes or a combination of both extremes may be responsible for the lower than expected BET surface area.

3.3.2 PXRD results

The PXRD of **P1** – **P5** are shown in Fig. 5. Close examination of the diffractograms indicates that they contain three distinct complexes. Comparing the simulated spectrum of $Zn_2(NH_2BDC)_2DABCO$ with **P5**, which exhibited the largest BET surface area of all the samples, indicates that **P5** consists primarily of crystalline $Zn_2(NH_2BDC)_2DABCO$.

As the surface area decreases, a series of amorphous peaks appear at 11.2 and 19.9° 2θ. Perhaps the most surprising sample is **P3**, which doesn't exhibit any evidence of $Zn_2(NH_2BDC)_2DABCO$, despite being porous.

Notably, in **P3** (and to a lesser degree in **P1** and **P2**) is the presence of sharp diffraction peaks that are inconsistent with the simulated diffractogram of $Zn_2(NH_2BDC)_2DABCO$. A search of Zn-BDC-containing moieties in the Cambridge Crystallographic Data Centre (CCDC) revealed that these two peaks match closely with the 1D zig-zag chain of $Zn(H_2O)_2(BDC)$ (Fig. 6). The slight differences in peak positions, towards larger distances (shorter angles), is consistent with an increase in the unit cell parameters due to the addition of the steric profile associated with the -NH_2 moiety.

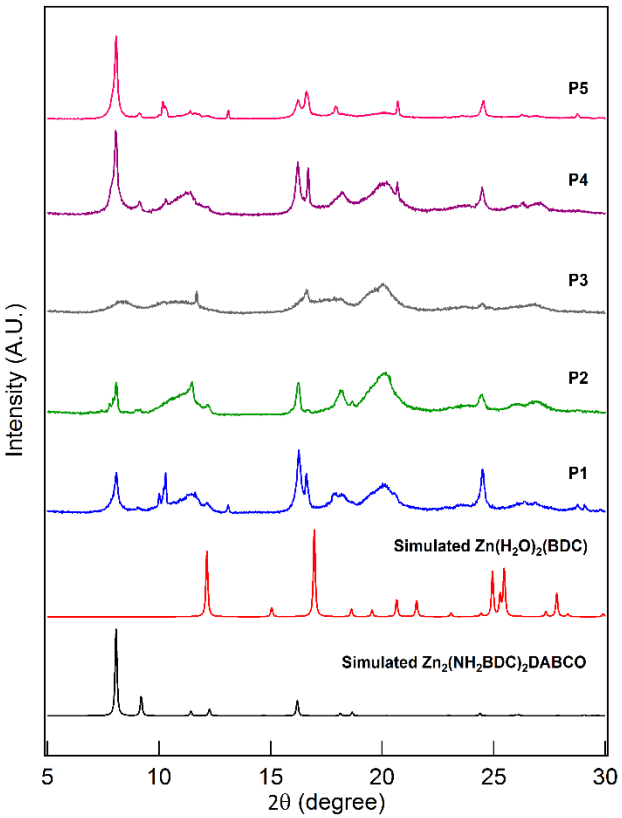

Fig. 5 PXRD spectra for **P1** – **P5** as well as the simulated PXRD for $Zn_2(NH_2BDC)_2DABCO$ (black) and $Zn(H_2O)_2(BDC)$ (red).

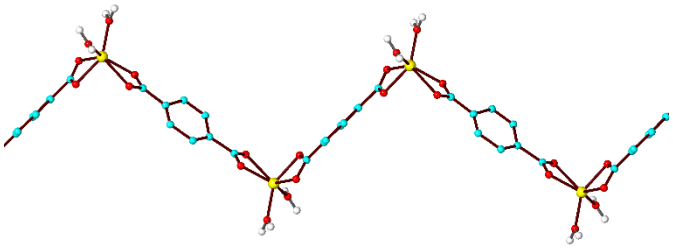

Fig. 6 1D zig-zag chains of 6-coordinate $Zn(H_2O)_2(BDC)$. Zinc (yellow), oxygen (red), carbon (blue), hydrogen (white).

4 Discussion

The synthesis of $Zn_2(NH_2BDC)_2DABCO$, in comparison to $Zn_2(BDC)_2DABCO$, has proven to be more complex than first anticipated. Simply substituting NH_2BDC for BDC results in gas adsorption isotherms of seemingly identical samples produced different BET surface areas as well as different types of hysteresis loops. Based on the characterization data, the products formed contain a uniform micropore consistent with $Zn_2(NH_2BDC)_2DABCO$, mesopores of various sizes, a linker ratio that is inconsistent with the expected linker ratio, and the presence of three different phases in the PXRD. Fig. 7 illustrates a mechanism of formation for $Zn_2(NH_2BDC)_2DABCO$ based on the present data.

We hypothesize that, initially, 1D chains of $Zn(H_2O)_2(BDC)$ form. This is in agreement with the PXRD of **P1** – **P3**, which show

the presence of non-porous $Zn(H_2O)_2(NH_2BDC)$ 1D chains (Fig. 5). Two of these 1D chains can come together (Fig. 7a) to form the 2D pillared paddlewheel sheets. These sheets are not expected to be porous as they would likely stack in an alternating fashion.[33,51] However, it is well established that paddlewheel sheets can pillar via a ditopic neutral linker such as DABCO. As this process happens, a porous material begins to form.

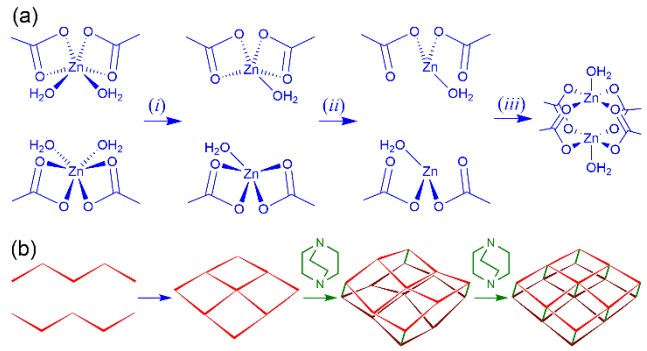

Fig. 7 (a) merging of 1D chains of $Zn(H_2O)_2(NH_2BDC)$ to form 2D paddlewheel sheets via (i) the dissociation of water, (ii) the breaking of intrachain Zn-carboxylate bonds, (iii) the formation of interchain Zn-carboxylate bonds. (b) a schematic illustrating how 1D chains can form 2D sheets followed by partial pillaring to form amorphous $Zn_2(NH_2BDC)_2DABCO$, followed by additional pillaring to form crystalline $Zn_2(NH_2BDC)_2DABCO$.

P3 is amorphous (Fig. 5) and porous (Fig. 4), with a PSD (Fig. 3) consistent with $Zn_2(NH_2BDC)_2DABCO$. Given these observations, we hypothesize that below a critical linker ratio – **P3** has the lowest NH_2BDC:DABCO linker ratio (Table 1). We hypothesize that $Zn_2(NH_2BDC)_2DABCO$ in **P3** is too flexible, resulting in the formation of an amorphous MOF (Fig. 5).[57-60] However, once a critical linker ratio is obtained, $Zn_2(NH_2BDC)_2DABCO$ begins to form a more rigid structure (**P5**, Fig. 5). Interestingly, as evident by the PXRD and NMR of **P5**, the critical linker ratio occurs at around 60% pillaring. Therefore, samples below this critical ratio contain a mixture of amorphous and crystalline $Zn_2(NH_2BDC)_2DABCO$.

5 Conclusions

Using a combination of surface area measurements, NMR spectroscopy, and powder X-ray diffraction, the mode of formation of $Zn_2(NH_2BDC)_2DABCO$ was presented. In total, evidence for a 1D chain of $Zn(H_2O)_2(NH_2BDC)$, amorphous $Zn_2(NH_2BDC)_2DABCO$, and crystalline $Zn_2(NH_2BDC)_2DABCO$ was observed. If control over the formation of the amorphous and crystalline materials can be achieved, then the role of linker defects and crystallinity on materials properties could be examined.

Conflicts of interest

There are no conflicts to declare.

Acknowledgements

The authors would like to acknowledge that Natural Science and Engineering Council of Canada (NSERC) for a Discovery Grant (MJK) and a Research Tools and Instrumentation grant (MJK). The authors would also like to acknowledge the Core Research Equipment & Instrument Training Network (CREAIT) at Memorial University for the use of their NMR and XRD facilities within the Centre for Chemical Analysis, Research and Training (C-CART) and The Earth Resources Research and Analysis Facility (TERRA) respectively. A special thanks to Dr. Céline Schneider for help with T1-relaxation analysis, as well as to Dr. Wanda Aylward for performing PXRD and SEM analysis.

Notes and references

1. H. Furukawa, K. E. Cordova, M. O'Keeffe and O. M. Yaghi, *Science*, 2013, **341**, 1230444.
2. A. U. Czaja, N. Trukhan and U. Muller, *Chem. Soc. Rev.*, 2009, **38**, 1284-1293.
3. Z. Hu, B. J. Deibert and J. Li, *Chem. Soc. Rev.*, 2014, **43**, 5815-5840.
4. S. Ma and H.-C. Zhou, *Chem. Commun.*, 2010, **46**, 44-53.
5. Y. H. Hu and L. Zhang, *Adv. Mater.*, 2010, **22**, 117-130.
6. S. Qiu, M. Xue and G. Zhu, *Chem. Soc. Rev.*, 2014, **43**, 6116-6140.
7. J.-R. Li, J. Sculley and H.-C. Zhou, *Chem. Rev.*, 2012, **112**, 869-932.
8. E. Barea, C. Montoro and J. A. R. Navarro, *Chem. Soc. Rev.*, 2014, **43**, 5419-5430.
9. R.-Z. Wu, X. Yang, L.-W. Zhang and P.-P. Zhou, *Dalton Trans.*, 2017, **46**, 9859-9867.
10. S. Gao, L. Zhao, L. Han, Z. Zhang and H. Zhao, *CrystEngComm*, 2018, **20**, 2237-2240.
11. I. Stassen, N. Burtch, A. Talin, P. Falcaro, M. Allendorf and R. Ameloot, *Chem. Soc. Rev.*, 2017, **46**, 3185-3241.
12. P. Kumar, A. Deep and K.-H. Kim, *Trends Anal. Chem.*, 2015, **73**, 39-53.
13. G. Huang, Y. Chen and H. Jiang, *Huaxue Xuebao*, 2016, **74**, 113-129.
14. J. Liang, Z. Liang, R. Zou and Y. Zhao, *Adv. Mater.*, 2017, **29**, 1701139.
15. Y. Liu, A. J. Howarth, J. T. Hupp and O. K. Farha, *Angew. Chem. Int. Ed. Engl.*, 2015, **54**, 9001-9005.
16. J. E. Mondloch, M. J. Katz, W. C. Isley III, P. Ghosh, P. Liao, W. Bury, G. W. Wagner, M. G. Hall, J. B. DeCoste, G. W. Peterson, R. Q. Snurr, C. J. Cramer, J. T. Hupp and O. K. Farha, *Nat. Mater.*, 2015, **14**, 512-516.
17. J. Liu, L. Chen, H. Cui, J. Zhang, L. Zhang and C.-Y. Su, *Chem. Soc. Rev.*, 2014, **43**, 6011-6061.
18. W. Lu, Z. Wei, Z.-Y. Gu, T.-F. Liu, J. Park, J. Park, J. Tian, M. Zhang, Q. Zhang, T. Gentle III, M. Bosch and H.-C. Zhou, *Chem. Soc. Rev.*, 2014, **43**, 5561-5593.
19. F. Moreau, D. I. Kolokolov, A. G. Stepanov, T. L. Easun, A. Dailly, W. Lewis, A. J. Blake, H. Nowell, M. J. Lennox, E. Besley, S. Yang and M. Schröder, *Proc. Natl. Acad. Sci.*, 2017, **114**, 3056-3061.
20. K. Sumida, D. L. Rogow, J. A. Mason, T. M. McDonald, E. D. Bloch, Z. R. Herm, T.-H. Bae and J. R. Long, *Chem. Rev.*, 2012, **112**, 724-781.

21. G. W. Peterson, M. R. Destefano, S. J. Garibay, A. Ploskonka, M. McEntee, M. Hall, C. J. Karwacki, J. T. Hupp and O. K. Farha, *Chem. Eur. J.*, 2017, **23**, 15913-15916.
22. X. Gao, R. Cui, G. Ji and Z. Liu, *Nanoscale*, 2018, **10**, 6205-6211.
23. F. Vermoortele, M. Vandichel, B. Van de Voorde, R. Ameloot, M. Waroquier, V. Van Speybroeck and D. E. De Vos, *Angew. Chem. Int. Ed.*, 2012, **51**, 4887-4890.
24. J. Lincke, D. Lässig, M. Kobalz, J. Bergmann, M. Handke, J. Möllmer, M. Lange, C. Roth, A. Möller, R. Staudt and H. Krautscheid, *Inorg. Chem.*, 2012, **51**, 7579-7586.
25. O. K. Farha, A. Özgür Yazaydın, I. Eryazici, C. D. Malliakas, B. G. Hauser, M. G. Kanatzidis, S. T. Nguyen, R. Q. Snurr and J. T. Hupp, *Nat. Chem.*, 2010, **2**, 944.
26. B. Li, Y. Zhang, D. Ma, T. Ma, Z. Shi and S. Ma, *J. Am. Chem. Soc.*, 2014, **136**, 1202-1205.
27. S. Yuan, L. Zou, H. Li, Y.-P. Chen, J. Qin, Q. Zhang, W. Lu, M. B. Hall and H.-C. Zhou, *Angew. Chem., Int. Ed.*, 2016, **55**, 10776-10780.
28. S. Yuan, Y.-P. Chen, J.-S. Qin, W. Lu, L. Zou, Q. Zhang, X. Wang, X. Sun and H.-C. Zhou, *J. Am. Chem. Soc.*, 2016, **138**, 8912-8919.
29. S. Yuan, W. Lu, Y.-P. Chen, Q. Zhang, T.-F. Liu, D. Feng, X. Wang, J. Qin and H.-C. Zhou, *J. Am. Chem. Soc.*, 2015, **137**, 3177-3180.
30. Y. Sun and H. C. Zhou, *Sci. Technol. Adv. Mater.*, 2015, **16**, 054202.
31. P. Deria, J. E. Mondloch, O. Karagiaridi, W. Bury, J. T. Hupp and O. K. Farha, *Chem. Soc. Rev.*, 2014, **43**, 5896-5912.
32. A. M. Shultz, A. A. Sarjeant, O. K. Farha, J. T. Hupp and S. T. Nguyen, *J. Am. Chem. Soc.*, 2011, **133**, 13252-13255.
33. O. Karagiaridi, W. Bury, J. E. Mondloch, J. T. Hupp and O. K. Farha, *Angew. Chem. Int. Ed.*, 2014, **53**, 4530-4540.
34. Z. Wang and S. M. Cohen, *J. Am. Chem. Soc.*, 2009, **131**, 16675-16677.
35. Z. Wang and S. M. Cohen, *Chem. Soc. Rev.*, 2009, **38**, 1315-1329.
36. Z. Wang, K. K. Tanabe and S. M. Cohen, *Chem. Eur. J.*, 2009, **16**, 212-217.
37. M. Savonnet, D. Bazer-Bachi, N. Bats, J. Perez-Pellitero, E. Jeanneau, V. Lecocq, C. Pinel and D. Farrusseng, *J. Am. Chem. Soc.*, 2010, **132**, 4518-4519.
38. M. C. Lawrence, C. Schneider and M. J. Katz, *Chem. Commun.*, 2016, **52**, 4971-4974.
39. B. J. Furlong and M. J. Katz, *J. Am. Chem. Soc.*, 2017, **139**, 13280-13283.
40. J. Zhang, G. B. White, M. D. Ryan, A. J. Hunt and M. J. Katz, *ACS Sustain. Chem. Eng.*, 2016, **4**, 7186-7192.
41. J. Zhang, J. B. De Coste and M. J. Katz, *Can. J. Chem.*, 2018, **96**, 139-143.
42. L. Shi, T. Wang, H. Zhang, K. Chang, X. Meng, H. Liu and J. Ye, *Adv. Sci.*, 2015, **2**, 1500006.
43. P. Serra-Crespo, E. V. Ramos-Fernandez, J. Gascon and F. Kapteijn, *Chem. Mater.*, 2011, **23**, 2565-2572.
44. W. Ma, L. Xu, Z. Li, Y. Sun, Y. Bai and H. Liu, *Nanoscale*, 2016, **8**, 10908-10912.
45. R. J. Marshall and R. S. Forgan, *Eur. J. Inorg. Chem.*, 2016, **2016**, 4310-4331.
46. M. W. Anjum, F. Vermoortele, A. L. Khan, B. Bueken, D. E. De Vos and I. F. Vankelecom, *ACS Appl. Mater. Interfaces*, 2015, **7**, 25193-25201.
47. Z. Wang, K. K. Tanabe and S. M. Cohen, *Inorg. Chem.*, 2009, **48**, 296-306.
48. J. Y. Lee, D. H. Olson, L. Pan, T. J. Emge and J. Li, *Adv. Funct. Mater.*, 2007, **17**, 1255-1262.
49. Z. Liang, M. Marshall and A. L. Chaffee, *Microporous Mesoporous Mater.*, 2010, **132**, 305-310.
50. D. A. Gómez-Gualdrón, P. Z. Moghadam, J. T. Hupp, O. K. Farha and R. Q. Snurr, *J. Am. Chem. Soc.*, 2016, **138**, 215-224.
51. D. N. Dybtsev, H. Chun and K. Kim, *Angew. Chem. Int. Ed.*, 2004, **43**, 5033-5036.
52. G. W. Peterson, J. B. DeCoste, F. Fatollahi-Fard and D. K. Britt, *Ind. Eng. Chem. Res.*, 2014, **53**, 701-707.
53. J. S. Grosch and F. Paesani, *J. Am. Chem. Soc.*, 2012, **134**, 4207-4215.
54. K. Biradha, A. Ramanan and J. J. Vittal, *Cryst. Growth Des.*, 2009, **9**, 2969-2970.
55. S. R. Batten and N. R. Champness, *Philos. Trans. Royal Soc. A*, 2017, **375**.
56. D. Britt, C. Lee, F. J. Uribe-Romo, H. Furukawa and O. M. Yaghi, *Inorg. Chem.*, 2010, **49**, 6387-6389.
57. T. D. Bennett and A. K. Cheetham, *Acc. Chem. Res.*, 2014, **47**, 1555-1562.
58. W. Li, M. R. Probert, M. Kosa, T. D. Bennett, A. Thirumurugan, R. P. Burwood, M. Parinello, J. A. K. Howard and A. K. Cheetham, *J. Am. Chem. Soc.*, 2012, **134**, 11940-11943.
59. S. A. Moggach, T. D. Bennett and A. K. Cheetham, *Angew. Chem., Int. Ed.*, 2009, **48**, 7087-7089.
60. P. Smart, C. A. Mason, J. R. Loader, A. J. H. M. Meijer, A. J. Florence, K. Shankland, A. J. Fletcher, S. P. Thompson, M. Brunelli, A. H. Hill and L. Brammer, *Chem. Eur. J.*, 2013, **19**, 3552-3557.

TOC Graphic

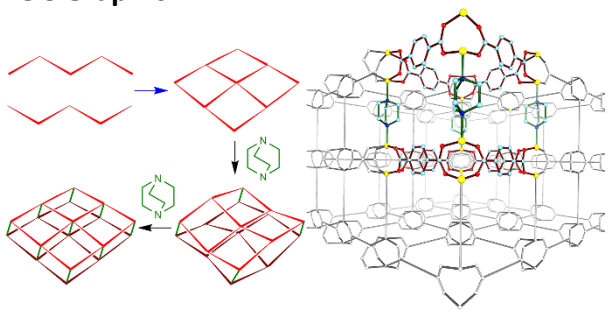

We examined the characterization data for $Zn_2(NH_2BDC)_2DABCO$ to gain mechanistic insight into the crystal engineering of pillared paddle-wheel MOFs.